The following publication Q. Zhao, S. Wang, J. Hu, H. Liu and H. K. Chu, "Controller Design for a Soft Continuum Robot With Concurrent Continuous Rotation," in IEEE/ASME Transactions on Mechatronics, vol. 29, no. 6, pp. 4504-4513, Dec. 2024 is available at https://doi.org/10.1109/TMECH.2024.3378274.

Controller Design for A Soft Continuum Robot with Concurrent Continuous Rotation

Qingxiang Zhao[1,2], Shuai Wang[2], Jian Hu[1,3], Hongbin Liu[1], Henry K. Chu[2], *Member IEEE*

***Abstract*—Soft continuum robot arms (CRAs) are potential in narrow confined spaces owing to the high dexterity and compliance, while torsional motion is also anticipated in some scenarios in addition to omni-directional bending. Most existing designs generate torsional motion either relying on an independent flexible shaft or with only limited rotation range. This work presented a control scheme for a fully self-rotatable CRA, enabling concurrent rotation along the deformable backbone while positioning the end effector. Shape configuration acts as a bridge between actuation inputs and tip pose, where the bending and rotation motions are decoupled in kinematics. With optimization-based algorithm and Jacobian-based online correction approach, the position of the tip could be well controlled and could cope with external disturbances. Both simulation and experiments demonstrate the effectiveness of the proposed model. Results indicate that the control scheme is applicable for conventional continuum robot designs and could also perform in-situ rotation, and the motion accuracy reached around $6mm$ for the $120mm$ length manipulator. A biopsy sampling experiment also demonstrates its potential in medical application.**

***Index Terms*—Continuum robot; Concurrent self-rotation and positioning; Jacobian-based correction; Constrained Optimization; Model Predictive Control**

I. Introduction

The presence of soft continuum robots opens a new way for manipulation in confined environments dexterously owing to their high compliance, safe contact and slender body. Various continuum robots have been applied in industrial inspection [1], pick and place [2], rescue [3] and minimally invasive surgery (MIS) [4]. Although the elongation/contraction of the secondary backbones could enable dexterous motion in serpentine task space, torsional motion is also desired especially for some surgical procedures, such as spine fusion [5], pelvic osteolysis treatment [6], and hip arthroplasty [7].

One typical solution to provide torsion along the deformable backbone is employing a flexible shaft passing through the instrument channel. In this case, the soft manipulator provides steerability and the channel follows the shape of the whole robot, which is categorized as direct rotation. Torsion transmission purely relies on the flexible shaft, and a motor connects its base end to generate torque [8]–[10]. The bending and rotation motions are decoupled. Replicable tools such as needle [11], drill bit [8], and forceps [12] could be mounted at the tip area for different surgical tasks. The flexible shaft brings additional stiffness to the continuum robots, leading to unnecessary bending, and on the other hand causes lubrication issue in rotation. Researchers have been working on developing rotation/twisting at the end effector. The inner-most tube of concentric tube robot [13] and co-axial push/pull robot [14] could twist at the tip, but due to the coupling between nested tubes, sweep may occur. In addition, the manoeuvrability of concentric tube robot will be reduced because its low stiffness is unable to cope with the elastic energy of the shaft [15]. Although tendon-driven or fluid-driven actuators [16] could somehow compensate the elastic force by regulating the robot's own stiffness [7], miniaturization is still challenging. Chen et. al [17] proposed a soft twisting pneumatic actuator, but the twisting only presents with several turns and the speed was also low.

To balance the tradeoff between dexterity and stiffness, Wang et al. [5] proposed an articulated surgical drill with distal stiffness and the distal dexterity is achieved using a geared rolling joint, where the stiffness reached $67.2N/mm$, but it also suffers limited bending dexterity and the distal segment could not adapt zigzag cavity. Ishii et al. [18] proposed a rotatable gripper with a novel double-screw-drive mechanism for laparoscopic surgery, and the rotation of the gripper was realized by a long rigid linkage. Black et. al [19] proposed a parallel cable-driven continuum robot with twisting motion at the tip. As a result, articulated linkages require complicated

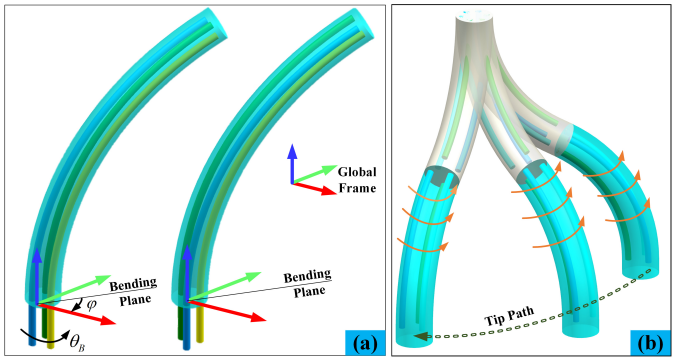

Fig. 1. (a) In-situ rotation: Robot base rotates towards the opposite direction of the direction angle generated by secondary backbone length variation ($\Delta\varphi = -\Delta\theta_B$), and the bending angle keeps unchanged. (b) Robot tip follows a path with concurrent RADB.

Qingxiang Zhao, Shuai Wang and Henry K. Chu are with the Department of Mechanical Engineering, Hong Kong Polytechnic University, Hong Kong, China (Corresponding author: Henry K. Chu. email: byron.wang@connect.polyu.hk; henry.chu@polyu.edu.hk).
Qingxiang Zhao, Jian Hu and Hongbin Liu are with the Centre for Artificial Intelligence and Robotics (CAIR) Hong Kong Institute of Science and Innovation, Chinese Academy of Sciences (email: Qingxiang.zhao@cair-cas.org.hk; hongbin.liu@cair-cas.org.hk).
Jian Hu is also with the Institute of Automation, Chinese Academy of Sciences. (email: hujian@cair-cas.org.hk)

transmission mechanism and much space.

Secondly, the entire soft manipulator is employed as a bendable and rotatable shaft to transmit torque to the tip, generating rotation along the deformable body (RADB) [20], which is categorized as indirect rotation. Shape Memory Alloy (SMA) was utilized as actuators to generate torsion and bending [21], [22], but heating and cooling request long time and the torsion angle is also limited. Kong et al. [23], [24] achieved concurrent torsion and bending by jointly rotating the base and steering the direction angle so that the robot performs in-situ rotation. The torsion range is limited because the electric cables of motors twine around the fixed parts while torsion angle exceeds $360°$, and it has only one segment. We have solved this problem by adding a slip ring at the robot base and used pneumatic regulators for actuation, enabling the dual-segment robot to perform continuous in-situ RADB [25]. As shown in Fig. 1 (a), in-situ rotation is achieved by rotating the robot base towards the opposite direction with the same angle as the variation of bending angle generated by secondary backbone length variation. Compared with the first design, RADB mechanism does not require specific instrument channel for rotation, but the bending and rotation is coupled, i.e. base rotation also leads to shape/tip configuration variation w.r.t. the global frame. TABLE. I lists and compares the two categories of rotation in continuum robotics.

Apart from structure design, the dexterity of soft CRA and torsion motion are both pursued through mathematic modelling. For the first design, bending and torsion are decoupled, requiring models for the robot motion and approaches to cope with the fluctuation caused by transmission shaft. The mapping between actuation inputs and shape/tip configuration of the manipulator was previously established based on Cosserat Rod theory [26], Pseudo-Rigid-Bar assumption [27], constant-curvature assumption [28], and data-driven approaches [29], [30]. Since the insertion of flexible shaft influences the steerability, stiffness regulation mechanism [31], [32] were proposed to against the disturbance. To balance between motion velocity and accuracy, dynamic modellings are required, such as Newton-Euler Equation [33] and Lagrange Equation [34], which need solvers [35] for the Partial Derivative Equations. For the RADB motion, the accuracy of CRAs deformation is key to realize accurate synchronization between base rotation and shape variation. The shape parameter variation between adjacent control instances is the focus in modelling, so that actuation inputs should be delicately computed to map with the shape. The hyper redundancy of soft robots essentially bring multiple solutions, opening the needs of an optimization-based method [36], [37].

Based on our previous work [25] proposing continuous in-situ RADB motion, this work focuses on achieving self-rotatable control for a dual-segment CRA, enabling concurrent deformation and RADB control. As illustrated in Fig. 1 (b), concurrent RADB and tip position motion are controlled accurately even if disturbance presents. The contribution of this work includes:

1) Optimization-based approach to decouple RABD and robot bending as they are coupled in hardware, enabling CRADB while following a desired 3D path.

2) Jacobian-based approach to correct the disturbance to enhance robot motion performance.

3) Model Predictive Control (MPC) scheme to follow consecutive path points while the future actual Jacobian is unknown.

The rest of this work is organized as follows. In Section II, we clarified the system design following the working principle of RADB motion and detailed the methodology of modelling. Simulation and experimental validation with different tasks were conducted and analyzed in Section III. Finally, Section IV concludes this work.

II. Prototype and Methodology

Since in-situ RADB is the synchronized motion of robot base rotation and direction angle variation actuated by bending actuators, the entire design considers continuous base rotation. Kinematics model should map between actuation inputs-tip position and actuation inputs-RADB angle, with which robot could perform RADB while following a 3D tip path.

A. Design and Prototype

To enhance dexterity and expand task space, a dual-segment CRA was mounted on a two-DoF platform, adding vertical translation DoF and rotation DoF at the proximal segment's base, as shown in Fig. 2 (a). Although the robot tip position is coupled with the orientation, the integration of the linear stage enlarges task space in z axis. The rotation DoF is beneficial for response in direction angle. The soft manipulator whose geometrical parameters are presented in Fig. 2 (b) was vertically hang on a slip ring (OUBAIBO, Dongguan, China), and the slip ring's rotor acts as a rotatable base for the soft manipulator. Thus, the tubes will not intertwine when the robot base rotation angle exceeds $360°$. The material of the robot is silicone (Ecoflex, 0020). It was fabricated using mold cast technology. Nylon thread passing through the central channel constrains the backbone length. Circumferential shallow spiral notches are also for configuring thread to limit radial expansion upon actuation. The proximal segment has six chambers, three of which are for actuation and the rest are for passing through the tubes actuating the distal segment. Each chamber is separately actuated by pressurized distilled water in which the bubble is ignorable as compared with pure water. Six linear stages with a pitch of $1mm$ were used to individually push/pull six syringes to precisely control the elongation/contraction of the secondary backbones, where the displacement of syringe's piston is used as bending actuation inputs. The two-DoF platform is accurately controlled by stepper motors, as can be seen in Fig. 2 (a). Fig. 2 (c) shows the basic task space of the robot, where the maximum bending angles were only $90°$ for illustration. It covers a dome shaped task space of around $75 \times 75 \times 50mm^3$ volume and the motion range of the linear stage is $0 \sim 100mm$. Four markers were attached at the midpoint and the tip to track the position of the two segments by RGB-D cameras (D435, Intel Realsense), and the tracked positions are deemed as ground truth for validation. Fig. 2 (d) shows the overall experimental setup.

Basically, in-situ RADB requires joint variation, i.e. $\Delta\theta_B = -\Delta\varphi$ (Fig. 1 (a)), while concurrent path following and RADB

TABLE I. Comparison about Rotation/Twisting in Soft Continuum Robotics

Rotation Category	Mechanism	Rotation	Characteristics
Direct Rotation	Concentric Tube Robot [13]	Continuous	Unnecessary Bending, Low Manoeuvrability
	Co-Axial Push/Pull Tube Robot [14]	Continuous	Multi-Section, Miniaturization
	Flexible Shaft for Transmission [8]–[10]	Continuous	2D Bending [10], One Section, Unnecessary Bending, Vibration, Ineffective Torque Transmission
	Shaped Memory Alloy [21], [22]	Limited Rotation	Long Time Cooling and Heating, High Stiffness
	Pneumatic Actuators [17]	Multi-turn Twisting	High Energy Density, Low Twisting Speed
	Articulated Linkages	Limited Rotation [19]	High Stiffness, Bulky
		Continuous [5], [18]	Large Stiffness
Indirect Rotation	Base Rotation and Direction Angle Variation Synchronization	Limited Rotation [23]	Cable Twining Issue, Coupled Rotation and Rotation
		Continuous [25]	Dual Section, Coupled Rotation and Rotation, Low Speed

need delicate modelling to bring the robot to the desired path points and present RADB angle.

B. Kinematics

To simplify modelling, the shape of the soft manipulator is assumed as two arcs connected in series, each of which is parametrized by direction angle (Ψ_1, φ_2) and bending angle (θ_1, θ_2). With the base rotation DoF, the actual direction of the proximal segment Ψ_1 is equal to $\theta_B + \varphi_1$, as illustrated in Fig. 3. Between adjacent control instances, RADB angle is $t = \min(|\Delta\theta_B|, |\Delta\varphi_1|)$.

Kinematics model is used to map between the actuation inputs $A \in R^{8\times1}$ and the tip position $P \in R^{3\times1}$ to reach a target position and simultaneously perform RADB angle t.

(1) FORWARD KINEMATICS Herein, we employed shape configuration (SC) as an bridge between the actuation inputs and the tip position, which is also a key to realize accurate RADB motion control. In building SC∼tip position mapping, the shape parameters generated by the bending actuators are: ${}^2S = [\varphi_1, \theta_1, \varphi_2, \theta_2]$, and the tip position w.r.t. frame $\{1\}$ is then solved via Homogenous Transformation:

$$\begin{aligned} {}^0P = {} & T_z(q_l)R_z(\Psi_1)T_x(r_1)R_y(\theta_1)T_x(-r_1)T_z(d) \\ & T_z(60^\circ + \varphi_2)T_x(r_2)R_y(\theta_2)T_x(-r_2) \end{aligned} \tag{1}$$

where T_j and R_j respectively denote translation and rotation transformation about j axis, and $r_i = \frac{l_i}{\theta_i}(i = 1, 2)$ is the bending radius of the ith segment. q_l is the vertical translation of the robot base. For abbreviation, the forward kinematics is expressed as: $[x, y, z] = F(q_l, \theta_B, \varphi_1, \theta_1, \varphi_2, \theta_2)$. Then, the mapping between ${}^2S$ and bending actuation inputs (except q_l and θ_B) could be initially established as:

$$\begin{aligned} \varphi_1 &= f_1(U_1) = \operatorname{atan2}(\sqrt{3}(u_2 - u_3), u_2 + u_3 - 2u_1) \\ \theta_1 &= g_1(U_1) = \kappa_1 \underbrace{\sqrt{u_1^2 + u_2^2 + u_3^2 - u_1u_2 - u_1u_3 - u_2u_3}}_{V_1}, \end{aligned} \tag{2}$$

where $U_1 = (u_1, u_2, u_3)$ denotes actuation configuration of the proximal segment, and κ_1 is a stiffness coefficient involved in robot material and geometry. Due to fabrication discrepancy and the pressurized fluid inside the actuation channels, the stiffness coefficient is not always a constant, which requires real-time tuning and will be detailed in Section II-C. For similarity and brevity, functions f_2 and g_2 for calculating φ_2 and θ_2 respectively are omitted. Since the base can provide larger and faster rotation motion, we require: $t_d = \Delta\theta_B$ and $|\Delta\theta_B| \le |\Delta\varphi_1|$.

(2) INVERSE KINEMATICS Then, actuation inputs $A = \{q_l, \theta_B, U_1, U_2\} \in R^{8\times1}$ are to be solved for a given desired position $P_d = \{x_d, y_d, z_d\}$, where the tip orientation is involved in the position and is not the focus in modelling. Since the robot is capable of configuring itself into multiple shapes to map with the given tip position P_d, this work will simplify the solving process to achieve the real-time control. The optimal shape configuration is needed to map with P_d.

Because of the redundancy, our algorithm first finds the shape ${}^1S_d = \{\Psi_{1d}, \theta_{1d}, \varphi_{2d}, \theta_{2d}\}$ to reach (x_d, y_d), and then the deviation in z axis will be compensated by the vertical DoF q_l:

$$q_l = z_d - z({}^1S_d), \tag{3}$$

where $z({}^1S_d)$ is the z coordinate obtained from the forward kinematics $F(0, 0, {}^2S_d)$. The robot base rotation angle $\theta_B(k)$ and corresponding $\varphi_1(k)$ are respectively solved: $\Delta\theta_B(k) = \theta_B(k+1) - \theta_B(k) = t_d$ and $\Delta\varphi_1(k) = \varphi_1(k+1) - \varphi_1(k) = \Psi_d - \Psi_1(k) + t_d$, where k denotes the kth control instance.

Specifically, Newton-Raphson method is utilized to find the optimal ${}^1S_d$, which is an iterative approach, i.e. in the jth iteration, S_j is updated as:

$$\begin{aligned} S_j &= S_{j-1} - \tfrac{G(S_{j-1}) - [x_d, y_d]^T}{J_G(S_{j-1})} \\ [x, y] &= G(\Psi_1, \theta_1, \varphi_2, \theta_2) \end{aligned} \tag{4}$$

where $J_G(S_{j-1})$ is the Jacobian of $G(\cdot)$, and $G(\cdot)$ maps between shape configuration and the tip position without vertical displacement q_l, i.e. $G(\Psi_1, \theta_1, \varphi_2, \theta_2) = F(0, 0, {}^2S)$. Only x, y coordinates are used for calculation. During iteration, the shape parameters are limited within proper ranges. In detail, Ψ_1 and φ_2 fall into the range of $[0, 2\pi]$, and the bending angles θ_1, θ_2 are both within $[\pi/10, 2\pi/3]$ to avoid buckling. If any element of S_n does not fall within the range, the algorithm will preset the value of this element to the mid-point of the range and continues the next solution. The iteration stops until the deviation reaches an acceptable value: $\left\|G({}^1S_j) - [x_d, y_d]^T\right\| \le \xi_{\max}$ or the iteration reaches the maximum steps. As a result, the desired shape is obtained as $S_d = S_j$.

After finding the proper shape parameters mapping with the tip position and the RADB angel, ${}^2S = [\varphi_1, \theta_1, \varphi_2, \theta_2]$ should be reached by the bending actuation inputs $[U_1, U_2]$. As shown in (2), it would not be easy to find the actuation inputs for there are three unknown variables and only two

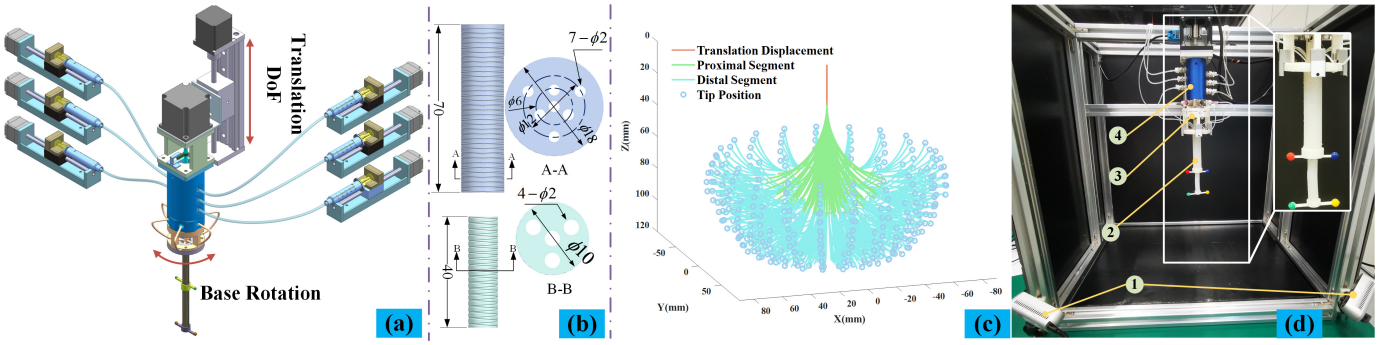

Fig. 2. (a) CAD model of the design. (b) Geometric dimension of each segment. (c) Task space illustration of the continuum robot. (d) Experimental setup. 1 RGB-D cameras; 2 Dual-segment soft continuum robot; 3 Slip ring.

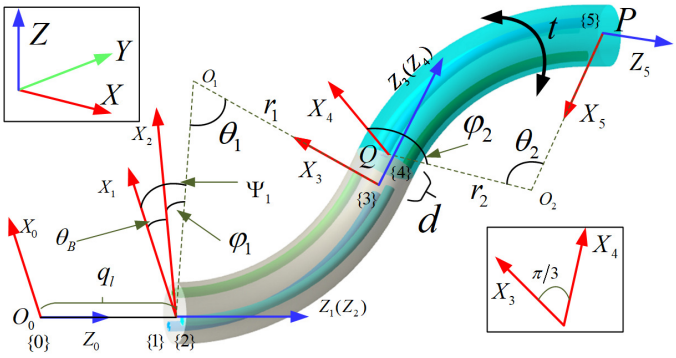

Fig. 3. Parametrized shape under PCC assumption. The tip position $P(x, y, z)$ w.r.t. the base frame $\{0\}$ is built. r is bending radius and Y axes are omitted.

equations. Therefore, we employed constrained optimization to solve $[U_1, U_2]$ for the given ${}^2S_d$ as:

$$\min \sum_{i=1}^{6} u_i \quad \text{s.t.} \begin{cases} \varphi_{1d} = f_1(U_1), \varphi_{2d} = f_2(U_2) \\ \theta_{1d} = g_1(U_1), \theta_{2d} = g_2(U_2) \\ u_{\min} \le u_i \le u_{\max} \end{cases}, \tag{5}$$

where $u_{\min}$ and $u_{\max}$ are respectively the lower and upper boundaries of the bending actuation inputs. The sum of all u_i is related to the amount of water inside the secondary backbones, and the stiffness coefficient is a variable that will be tuned through actual Jacobian matrix. To speed up the optimization process and avoid the infinite value in atan2() function, we employed sequential quadratic programming algorithm to find the optimal actuation inputs (MATLAB 2019b Constrained Optimization Toolbox *fmincon*).

C. Jacobian-based Online Correction

When the desired shape parameters are evaluated through the Newton-Raphson algorithm, the required actuation inputs are then computed using (5), but fabrication discrepancy and external disturbance both cause inaccuracy to the inverse kinematics. Thereby, the direction angle and bending angle should be tuned during robot motion. We proposed Jacobian-based online correction method. By comparing the deviation between actual Jacobian obtained by the real shape configuration and the theoretical one calculated from (2), function $f(\cdot)$ and $g(\cdot)$ are then tuned adaptively. Taking the proximal segment as an example, we could find the real shape parameters φ_{1a} and θ_{1a} by the real tip position $Q_a = (x_a^Q, y_a^Q, z_a^Q)$ tracked by the RGB-D cameras:

$$\begin{aligned} \varphi_{1a} &= \text{atan2}(y_a^Q, x_a^Q) \\ 1 - \cos(\theta_{1a}) &= \frac{\theta_{1a} x_a^Q}{l_1 \cos(\varphi_{1a})} \end{aligned} \tag{6}$$

where l_1 is the backbone length of the proximal segment, and θ_{1a} is solved via *fzero*() in MATLAB. The real Jacobian matrix of the robot will be evaluated online and used to iteratively update (2). By approximating the dual-segment robot through piecewise constant curvature assumption, the deviation between the actual Jacobian J_k^a and the theoretical Jacobian J_k^t could update (2) as:

$$\begin{cases} f_k = f_k^t + (J_k^a(1) - J_k^t(1))(U(k) - U(k-1)) \\ \kappa_k = \kappa_{k-1} + \frac{(J_k^a(2) - J_k^t(2))(U(k) - U(k-1))}{V_1(k)} \end{cases} \tag{7}$$

where $J_k^a(i)$ denotes the ith row of the matrix, and $J_k^t(i)$ is the theoretical Jacobian matrix. The correction for the two segments is identical, so it is omitted for the distal segment.

D. Optimization using Model Predictive Control

After correcting and updating the robot kinematics, a control scheme can be implemented to further optimize the control inputs. When the robot is commanded to follow a path, a series of immediate points are then generated.

In implementation, let Φ denote a series of desired shape configurations to follow, and the controller should be designed to minimize the error between Φ_k and S_k with the Jacobian matrix J_k. The predicted tip configuration $S_{k+1|k}$ under current S_k is: $S_k + J_k \Delta U_k$. In predictive control, the tip configuration in further instance is also predicted as: $S_{k+m|k} = S_k + \sum_{i=k}^{n} J_i \Delta U_i$, where m and n are respectively predictive horizon and control horizon ($n \le m$). Herein, we set $n = m$, and the control sequence is organized as:

$$\Im = \Upsilon + \Re \Delta \Theta, \tag{8}$$

where

$$\begin{aligned}\Im &= \left[S_{k+1|k}, \cdots, S_{k+n|k}\right]^T \\ \Upsilon &= \left[S_k, \cdots, S_k\right]^T \\ \Re &= \begin{bmatrix} J_k & \cdots & 0 \\ \cdots & J_{k+1} & 0 \\ J_k & \cdots & J_{k+n} \end{bmatrix} \\ \Delta\Theta &= \left[\Delta U_k, \cdots, \Delta U_{k+n}\right]^T.\end{aligned} \tag{9}$$

Since we are only able to obtain J_k at instance k, the Jacobian in all future instances are calculated using the theoretical value and the control horizon n is set smaller, ensuring the robot can accurately move to subsequent given shape configurations. Through receding horizon control theory, the controller can update its current Jacobian and actuation inputs to bring the robot tip into the desired shape configuration. Then, the problem is to solve the optimal actuation sequence $\Delta\Theta$, which is to minimize the error between $\Im$ and Φ, so the cost function is built as:

$$L = (\Im - \Phi)^T(\Im - \Phi) + \Delta\Theta^T R\Delta\Theta, \tag{10}$$

where $R_{n\times n}$ is a diagonal weighting matrix tuning bending actuation inputs. A larger R means assigning a lower cost to the bending actuation inputs. Additionally, constraints should be set on $\Delta\Theta$ to avoid buckling. Now, it is a problem of Quadratic Programming with constraints:

$$\begin{aligned}&\Delta\Theta = \arg\min_{\Delta\Theta} (\Im - \Phi)^T(\Im - \Phi) + \Delta\Theta^T R\Delta\Theta \\ &\text{w.r.t. :} \Delta U_{\min} \le \Delta U \le \Delta U_{\max}\end{aligned}. \tag{11}$$

Lagrangian algorithm was employed to solve the optimal bending actuation inputs. The complete methodology is detailed in Algorithm 1.

Algorithm 1: Methodology

Input: M path points $P = P_d(1), \cdots, P_d(M)$
Max. SC deviation $\xi_{\max}$, Control horizon n,
$U_{\max}, U_{\min}$, RADB angle t_d
Result: Move to each P with RADB angle t_d between adjacent instances

```
// Calculate each SC
```
foreach $i \in M$ **do**
  Initialize j
  while $\left\| G(S_j) - [x_d, y_d]^T \right\| \le \xi_{\max}$ **do**
    $S_j \leftarrow S_{j-1} - \frac{(G(S_{j-1}) - [x_d, y_d]^T)}{J_G(S_{j-1})}$
    $j \leftarrow j + 1$
  end
  $S_i \leftarrow S_j$
end
```
// Move to each SC
```
foreach $i \in (M - n)$ **do**
  Calculate q_l using (3)
  Optimize $\Delta\Theta$ using (11)
  Calculate $[U_{i+1}, \cdots, U_{i+n}]$ and Actuate
  $i \leftarrow i + n$
  Sense the real ${}^2S_n$ by vision system
  Calculate J_n^t and J_n^a
  Correct kinematics using (7)
end

III. Simulation and Experimental Validation

The modelling and control strategy are first tested in simulation to find the optimal parameters for further experimental validation. The two RGB-D cameras were respectively calibrated and the coordinates were aligned w.r.t. the base frame $\{0\}$, and the collected tip positions are deemed as ground truth. To find the basic robot response, we set different actuation inputs and calculated the corresponding shape parameters for each segment when the robot was stable. In between actuation instances, the bending actuation inputs increased or decreased $0.5mm$ randomly. When the elongation of the secondary backbone was below $4mm/1.5mm$ (proximal/distal segment), the shape parameters varied slightly and when it is larger than $13mm/6mm$, the bending angles exceeded $150°$. Therefore, we limit the minimal bending actuation inputs to $4mm/1.5mm$ and the maximum to $13mm/6mm$ for the proximal/distal segments. Within the range, the mean values of the coefficients κ_1 and κ_2 were respectively evaluated using least square method to be 0.07 and 0.16. Additionally, the actual direction angle also deviated with the theoretical value, which is generally the fabrication discrepancy, demonstrating the necessity to correct the kinematics.

A. Simulation and System Setting

Two simulation tasks were designed to initially test the performance of the proposed methodology and to find the basic parameters of the algorithm.

(1) Point-to-Point movement

The destination of the tip was set to $P_d = [30, 50, 160]^T$ (unit: mm) and the initial bending actuation inputs were $[U_1, U_2] = [10, 10, 0, 0, 3, 0]$. The two stepper motors were deactivated, i.e. $q_l = \theta_B = 0$. The tip position in the first instance was $P(1) = [-32.89, -39.68, 104.57]^T$. We set the step distance to $6mm$, so that the robot stops when the deviation between current tip position and the destination is smaller than this value, leading to an acceptable percentage of position error/backbone length ($6/120 = 5\%$). Robot tip was always commanded to move to a planned position in each instance using the step distance. In simulation, the stiffness coefficients were not tuned adaptively for the fabrication discrepancy was not considered. Before implementing the task, Newton-Raphson method for solving the shape parameters was tested to investigate the feasibility and to find the optimal iteration steps. $\xi_{\max}$ was set to $3mm$, and for the 11 tip positions, the shape parameters can be searched within 6 iterations, taking $0.2s$ maximumly (MATLAB 2019b), so the stopping criterial is: $\xi_{\max} \le 3mm$ or the maximum iteration reaches 8.

In the simulation, the RADB angle was first set to $t_d = 10°$ to see the basic performance, and the result is shown in Fig. 4 (a), from which the deviation between actual path points and the planned is far smaller than $0.1mm$. The time cost

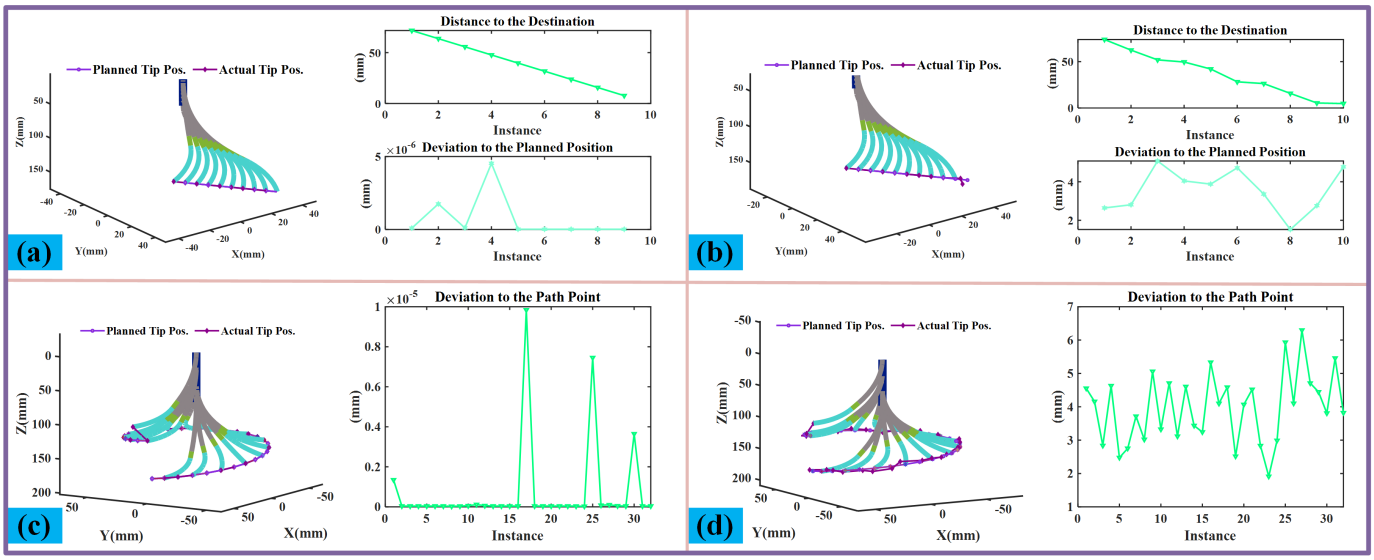

Fig. 4. Simulation results. (a)/(b) Point-to-point movement in free/disturbed condition ($t_d = 10°$). (c)/(d) 3D path-following task with RADB in free/disturbed condition ($t_d = 10°$).

of (5) was less than $0.1s$ in each instance. The deviation between current tip position to the goal decreased almost linearly, and the result theoretically demonstrates the feasibility of the proposed modelling approach. Then, to mimic the presence of external disturbance, we manually added a random error of $4mm$ to the tip position in each control instance: $P(k) \leftarrow P(k) + \delta^{3\times1}, \delta \in [-4, 4]$, and the corresponding results are shown in Fig. 4 (b). This also proves that the kinematics model could cope with external disturbance while simultaneously performing CRADB. It should be noted that the robot was only commanded to the next planned position, so that the MPC model was deactivated.

(2) PATH-FOLLOWING TASK

Then, a 3D elliptical path (long axis $130mm$, short axis $90mm$, height variation: 130 to 180) with 32 path points was then employed to follow. The control horizon was set to 4. The first actuation inputs were $[0, 0, 0, 9, 7.5, 0, 5, 5]$, with which the tip position was beside the first path point. The system then started to reach these path points one by one. Fig. 4 (c) shows the results in load-free condition, where the rotation angle t_d was also $10°$. Also, the actual tip position of each point follows well with the given values, which further shows that the proposed algorithm enables accurate path following with concurrent RADB. Similarly, the task was then tested in disturbed condition, and the results are shown in Fig. 4 (d). The maximum deviation was about $6mm$, which was within the acceptable error range. Although the two categories of simulation tasks initially tested the feasibility of the proposed methodology, fabrication discrepancy was not considered, requiring more validation through experiments.

B. Experiments

The control horizon and other parameters in methodology are all identical as those in simulation. It should be noted that the accuracy of tip position is the key factor of this work in modelling, and the system is operating at a slow speed (quasi-static motion). To ensure tracking accuracy, the vision system sampled the markers' position 5 times and calculated the mean value 1.5 seconds after actuating the robot. To minimize the inertial effect, the rotation velocity of the base was set to $60rpm$ in testing. The results were all recorded in supplementary videos.

(1) SHAPE CONTROL WITH/WITHOUT BASE ROTATION

The proposed design and method also cover the function of conventional designs that the soft manipulator only deforms with four DoFs (two bending angles and two direction angles) while the two-DoF platform is not activated. To illustrate the basic function, the two segments were commanded to follow a series of shape parameters using the bending actuation search algorithm (4). The actuation inputs at the first instance were set to $[0, 0, 0, 10, 10, 0, 5, 0]$ and the corresponding shape parameters were obtained by the vision system, where Jacobian-based correction method was not employed to basically investigate the motion accuracy. The direction angle of the proximal segment was required to decrease $20°$ ($\Delta\theta_B = 16°, \Delta\varphi_1 = 4°$) and the bending angles kept constant between two adjacent instances. Fig. 5 (a) shows the comparison between the theoretical tip positions and the actual path. It can be seen from the results that the actual path points follow well with the desired, and the maximum position error is around $5mm$.

For comparison, the base DoFs were not activated, so the shape was only controlled by the bending actuators. It was also commanded to follow the shape configurations. The theoretical tip position and the actual path points are shown in Fig. 5 (b), where the maximum position error was around $3mm$. The maximum error was smaller than that with base rotation, which is due to inertial effect during base rotation. But the base rotation could indeed reduce the motion range of the bending actuators, indicating the merit of the rotation DoF at the base.

(2) POINT-TO-POINT MOVEMENT TASK

The success of the above experiments provides founda-

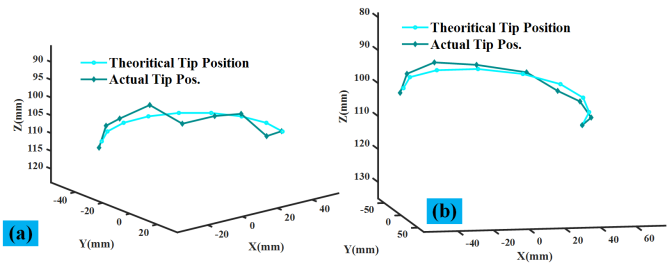

Fig. 5. Comparison between base rotation and base deactivated modes. (a) Base rotation. (b) Without base rotation DoF.

tion to validate point-to-point movement tasks, where multiple RADB angles were set. At first, the actuation inputs were set to $[0, 0, 10, 10, 0, 0, 4.5, 0]$ with the tip position of $[-34.2, 36.8, 105]$, and the destination was $[30, 50, 150]$. The RADB angle were respectively set to $(0°, -10°, 5°, 10°)$. The tip path for the four settings are shown in Fig. 6 (a) and recorded in the supplementary video. Taking the tip path of $t_d = 0°$ as reference, the deviation of the path points for each setting was calculated and plotted in Fig. 6 (b). The position deviation was below $4mm$ when $t_d = 5°$. With the increase of t_d, the error increases because Jacobian maps in local area. The snapshots of the robot are shown in Fig. 6 (c). The shapes of $t_d = 0°$ and $t_d = 5°$ settings are almost same, but the positions of the markers differed in each instance, showing the presence of the RADB motion.

To test the performance of processing external disturbance, a nut of $8.6g$ was hung at the robot tip and the t_d was set to $10°$ for this point-to-point movement task. As a result, the position errors of the proximal segment and the distal segment were respectively around $5mm$ and $10mm$. The lower stiffness of the distal segment could not process the external force caused by the load very well so the error reached $10mm$, as shown in Fig. 6 (c) (downmost). On the contrary, the error of the proximal segment is almost comparable with that in load-free condition, showing that the control scheme could adaptively process the disturbance.

(3) 3D PATH-FOLLOWING TASK

We also designed an elliptical 3D path with 32 path points, where the desired path is identical with that in simulation. The RADB angle t_d was set to $10°$, and the actual tip path is shown in Fig. 7 (a). Fig. 7 (b) illustrates the position error in each instance, from which the maximum error is around $7mm$ and the mean value is around $4mm$. The maximum position error presented at the leftmost of the elliptical path points, where the inertial effect left significant influence on the distal segment and the fabrication discrepancy affects the accuracy severely. This shows that the proposed design and method enables concurrent tip path following and CRADB. Additionally, the vertical translation DoF works well with the bending actuators, compensating the z value between the desired and that only due to the bending actuators, as could be observed in the supplementary video.

(4) IN-SITU ROTATION

Apart from RADB while following a given path, each segment

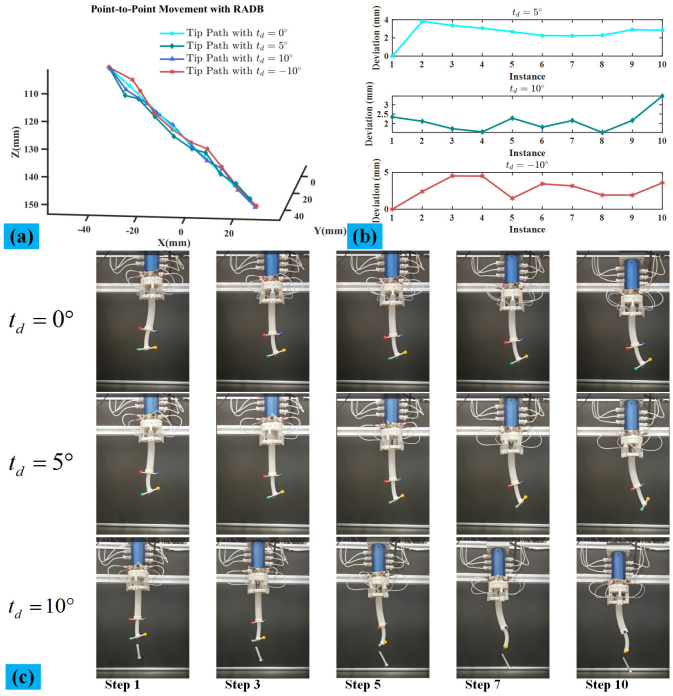

Fig. 6. Point-to-point movement results. (a) Tip path with different RADB settings. (b) Tip deviation with the planned path points in different scenarios. (c) Snapshots of the robot.

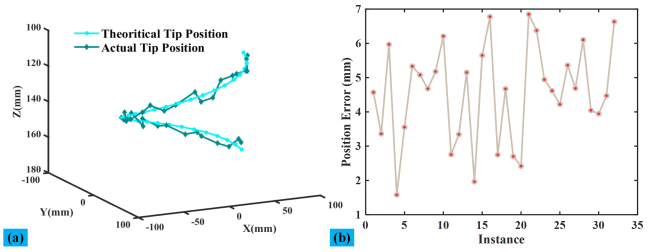

Fig. 7. (a) 3D path-following task result. RADB angle was $t_d = 10°$. (b) Position error in each control instance.

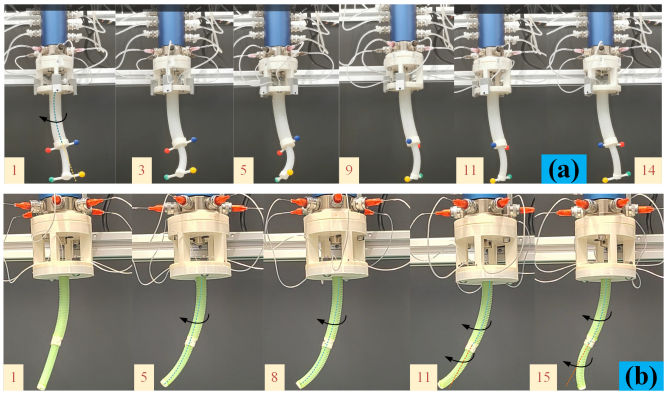

Fig. 8. (a) RADB of the proximal segment and fixed rotation of the distal segment. (b) In-situ rotation of the new lighter continuum robot arm. The subscript denotes the control instance number. The subscripts denote the number of control instance.

could also perform in-situ rotation. First, the two segments were commanded to perform individual rotation, i.e. the proximal segment rotates along the deformed backbone and the distal rotates about a fixed axis (axis Z_4 in Fig. 3). The actuation inputs in the first instance was set to $[30, 0, 4, 12, 4, 2.3, 3.4, 0]$. The bending angles of the two segments were always kept constant, and we set: $\Delta\theta_B(k) = -\Delta\varphi_1(k)$ and $\varphi_2(k+1) = \varphi_2(k) + 10^\circ$. After calculating the shape parameters of each segment, the robot was then commanded to rotate 10° for the following 18 instances. Fig. 8 (a) shows the snapshots of robot in some instances, and the full motion was recorded in the supplementary video. As a result, the tip of the proximal segment almost kept constant, and in-situ rotation was finally achieved. The red marker and the blue marker always rotated about the proximal segment's tip, and the shape of it also kept unchanged. Vision system captured their positions in each instance, and the result shows that the maximum fluctuation of the tip was about $3mm$, which was due to the gravitational force of the distal segment. On the other hand, the distal segment rotated 180° about Z_4 axis. The rotation accuracy of the distal segment quantified by roundness was about $4mm$, which is due to inertial effect and fabrication discrepancy.

To eliminate the gravitational effect of the distal segment, we have fabricated a new continuum robot arm, which has $9mm$ and $7mm$ diameters for the proximal segment and the distal, respectively. We used the new one to conduct in-situ rotation again to test the performance. Also, 18 control instances were employed. In the previous 9 instances, the whole robot arm performed in-situ rotation, and in the subsequent 9 instances the distal segment rotated about the fixed axis for comparison. Fig. 8 (b) shows the snapshots of the rotation motion, and the tip position accuracy reached $4mm$. From the result, the shape of the proximal segment almost kept unchanged, and the distal segment moved as desired.

(5)BIOPSY SIMULATION

The proposed design and method have been well validated, and the concept is potential in medical application. For soft tissue, conventional biopsy forceps could directly collect the sample, while it is difficult for the hard tissues. We first used the slender soft continuum robot to perform biopsy procedure, and the setup is shown in Fig. 9 (a-1). A pathological esophagus model was placed within the robot task space. Plasticine acts as the to be collected samples at an anabrosis area. As can be seen from Fig. 9 (a-2) to Fig. 9 (a-4), the robot gradually reached the port and then passed the tumour to get the anabrosis area. Finally, one biopsy forceps (GM-FB-C-N-10-1200, OD: 1.0mm, GRIT, China) configured at the central instrument channel successfully collected the plasticine. In the whole process, only the bending and feed/retraction motions were used for the soft plasticine.

We then changed the sample as relatively hard plasticine, so that opening/closing of the forceps may not be able to get the sample, requiring RADB motion. The hard plasticine was filled into a silicone tube, as shown in Fig. 9 (b). Initially, the robot approached the task area, and it started to perform RADB after closing the forceps, as shown in Fig. 9 (b-2). From Fig. 9 (b-3) to Fig. 9 (b-6), the forceps were commanded to rotate about the silicone tube, with 10° increase between steps. Through 180° rotation along the deformed shape and retraction (see Fig. 9 (b-7)), the robot collected much sample. It further demonstrates the applicability of the proposed design and method.

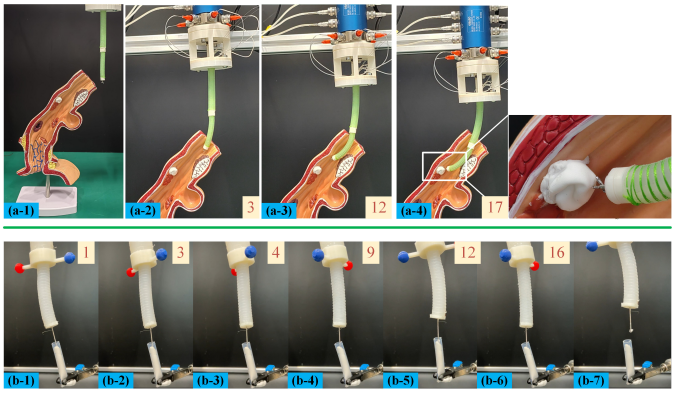

Fig. 9. Biopsy simulation demonstration. (a) The robot explored a pathological esophagus model and a biopsy forceps collected samples. (b) RADB motion promotes easier sample collection. The subscripts denote the number of control instance.

IV. CONCLUSION

In this work, a novel continuum robot which can provide concurrent rotational motion along the deformable backbone and bending motion was proposed, offering an additional capability as compared to conventional continuum robot designs. The dual-segment soft manipulator has two additional DoFs, rendering higher dexterity and larger task space. With the robot base rotation and synchronization with bending actuators, RADB motion could also be achieved while positioning the manipulator simultaneously. Although the added 2-DoF platform increased the essential redundancy, the proposed modelling strategy decoupled bending and base movement. With the optimization-based approach, a feasible shape configuration was first searched to map with the desired tip position. Then, constrained optimization algorithm searched the bending actuation inputs and Jacobian-based approach adaptively tunes the shape parameter $\sim$ actuation inputs mapping. For path-following tasks, Model Predictive Control scheme was employed. Results show that the robot has successfully realized concurrent RADB and positioning, and the accuracy is around $6mm$ (5% of error-to-length ratio) in quasi-static condition. Due to the inertial effect caused by base rotation, the accuracy of the setting without base rotation is higher than that in rotation mode. In the experimental demonstration, significant vibration was observed due to the low stiffness of the robot, leading to poor dynamic performance. The actual tip position could be directly obtained by the vision, which may not be applicable in confined environment. In the future, we will continue to enhance its motion accuracy through dynamic modelling, requiring collecting acceleration and velocity of the manipulator. Some embedded proprioceptive sensors will also be developed.

REFERENCES

[1] M. Wang, X. Dong, W. Ba, A. Mohammad, D. Axinte, and A. Norton, "Design, modelling and validation of a novel extra slender continuum robot for in-situ inspection and repair in aeroengine," *Robotics and Computer-Integrated Manufacturing*, vol. 67, p. 102054, 2021.

[2] S. Kolachalama and S. Lakshmanan, "Continuum robots for manipulation applications: a survey," *Journal of Robotics*, vol. 2020, 2020.

[3] Y. Yamauchi, Y. Ambe, H. Nagano, M. Konyo, Y. Bando, E. Ito, S. Arnold, K. Yamazaki, K. Itoyama, T. Okatani, H. G. Okuno, and S. Tadokoro, "Development of a continuum robot enhanced with distributed sensors for search and rescue," *ROBOMECH J.*, vol. 9, no. 1, dec 2022.

[4] W. Hong, F. Feng, L. Xie, and G.-Z. Yang, "A Two-Segment Continuum Robot With Piecewise Stiffness for Maxillary Sinus Surgery and Its Decoupling Method," *IEEE/ASME Trans. Mechatronics*, pp. 1–11, mar 2022.

[5] Y. Wang, H.-W. Yip, H. Zheng, H. Lin, R. H. Taylor, and K. W. S. Au, "Design and experimental validation of a miniaturized robotic tendon-driven articulated surgical drill for enhancing distal dexterity in minimally invasive spine fusion," *IEEE/ASME Transactions on Mechatronics*, vol. 26, no. 4, pp. 1858–1866, Aug 2021.

[6] S. Sefati, R. Hegeman, F. Alambeigi, I. Iordachita, P. Kazanzides, H. Khanuja, R. H. Taylor, and M. Armand, "A surgical robotic system for treatment of pelvic osteolysis using an fbg-equipped continuum manipulator and flexible instruments," *IEEE/ASME Transactions on Mechatronics*, vol. 26, no. 1, pp. 369–380, 2021.

[7] A. N. B. A. Fuad, H. Elangovan, K. Deep, and W. Yao, "A robotic flexible drill and its navigation system for total hip arthroplasty," *Annals of Biomedical Engineering*, vol. 46, pp. 464 – 474, 2017.

[8] F. Alambeigi, Y. Wang, S. Sefati, C. Gao, R. J. Murphy, I. Iordachita, R. H. Taylor, H. Khanuja, and M. Armand, "A Curved-Drilling Approach in Core Decompression of the Femoral Head Osteonecrosis Using a Continuum Manipulator," *IEEE Robot. Autom. Lett.*, vol. 2, no. 3, pp. 1480–1487, 2017.

[9] J. H. Ma, S. Sefati, R. H. Taylor, and M. Armand, "An active steering hand-held robotic system for minimally invasive orthopaedic surgery using a continuum manipulator," *IEEE Robotics and Automation Letters*, vol. 6, no. 2, pp. 1622–1629, 2021.

[10] N. Tan, X. Gu, and H. Ren, "Design, characterization and applications of a novel soft actuator driven by flexible shafts," *Mechanism and Machine Theory*, vol. 122, pp. 197–218, 2018.

[11] X. Xiao, Y. Wu, Q. Wu, and H. Ren, "Concurrently bendable and rotatable continuum tubular robot for omnidirectional multi-core transurethral prostate biopsy," *Med. Biol. Eng. Comput.*, vol. 60, no. 1, pp. 229–238, jan 2022.

[12] T. Li, L. Qiu, and H. Ren, "Distributed Curvature Sensing and Shape Reconstruction for Soft Manipulators with Irregular Cross Sections Based on Parallel Dual-FBG Arrays," *IEEE/ASME Trans. Mechatronics*, vol. 25, no. 1, pp. 406–417, 2020.

[13] S. Sharma, T. G. Mohanraj, J. P. Amadio, M. Khadem, and F. Alambeigi, "A concentric tube steerable drilling robot for minimally invasive spinal fixation of osteoporotic vertebrae," *IEEE Transactions on Biomedical Engineering*, vol. 70, no. 11, pp. 3017–3027, 2023.

[14] K. Oliver-Butler, J. A. Childs, A. Daniel, and D. C. Rucker, "Concentric push–pull robots: Planar modeling and design," *IEEE Transactions on Robotics*, vol. 38, no. 2, pp. 1186–1200, 2022.

[15] T. Liu, G. Zhang, P. Zhang, T. Cheng, Z. Luo, S. Wang, and F. Du, "Modeling of and experimenting with concentric tube robots: Considering clearance, friction and torsion," *Sensors*, vol. 23, no. 7, p. 3709, 2023.

[16] X. Peng, N. Zhang, L. Ge, and G. Gu, "Dimension optimization of pneumatically actuated soft continuum manipulators," in *2019 2nd IEEE International Conference on Soft Robotics (RoboSoft)*. IEEE, 2019, pp. 13–18.

[17] F. Chen, Y. Miao, G. Gu, and X. Zhu, "Soft twisting pneumatic actuators enabled by freeform surface design," *IEEE Robotics and Automation Letters*, vol. 6, no. 3, pp. 5253–5260, 2021.

[18] C. Ishii, K. Kobayashi, Y. Kamei, and Y. Nishitani, "Robotic forceps manipulator with a novel bending mechanism," *IEEE/ASME Transactions on Mechatronics*, vol. 15, no. 5, pp. 671–684, 2009.

[19] C. B. Black, J. Till, and D. C. Rucker, "Parallel continuum robots: Modeling, analysis, and actuation-based force sensing," *IEEE Transactions on Robotics*, vol. 34, no. 1, pp. 29–47, 2018.

[20] N. Simaan, K. Xu, W. Wei, A. Kapoor, P. Kazanzides, R. Taylor, and P. Flint, "Design and integration of a telerobotic system for minimally invasive surgery of the throat," *The International journal of robotics research*, vol. 28, no. 9, pp. 1134–1153, 2009.

[21] J. Sheng, D. Gandhi, R. Gullapalli, J. M. Simard, and J. P. Desai, "Development of a meso-scale sma-based torsion actuator for image-guided procedures," *IEEE Transactions on Robotics*, vol. 33, no. 1, pp. 240–248, 2016.

[22] J.-E. Shim, Y.-J. Quan, W. Wang, H. Rodrigue, S.-H. Song, and S.-H. Ahn, "A smart soft actuator using a single shape memory alloy for twisting actuation," *Smart Materials and Structures*, vol. 24, no. 12, p. 125033, 2015.

[23] Y. Kong, S. Song, N. Zhang, J. Wang, and B. Li, "Design and kinematic modeling of in-situ torsionally-steerable flexible surgical robots," *IEEE Robotics and Automation Letters*, vol. 7, no. 2, pp. 1864–1871, 2022.

[24] Y. Kong, J. Wang, N. Zhang, S. Song, and B. Li, "Dexterity analysis and motion optimization of in-situ torsionally-steerable flexible surgical robots," *IEEE Robotics and Automation Letters*, vol. 7, no. 3, pp. 8347–8354, 2022.

[25] Q. Zhao, J. Lai, X. Hu, and H. K. Chu, "Dual-segment continuum robot with continuous rotational motion along the deformable backbone," *IEEE/ASME Transactions on Mechatronics*, 2022.

[26] G. Wu and G. Shi, "Design, modeling, and workspace analysis of an extensible rod-driven Parallel Continuum Robot," *Mechanism and Machine Theory*, vol. 172, 2022.

[27] C. Wang, C. G. Frazelle, J. R. Wagner, and I. Walker, "Dynamic Control of Multi-Section Three-Dimensional Continuum Manipulators Based on Virtual Discrete-Jointed Robot Models," *IEEE/ASME Transactions on Mechatronics*, vol. 26, no. 2, pp. 777–788, 2020.

[28] M. Srivastava, J. Ammons, A. B. Peerzada, V. N. Krovi, P. Rangaraju, and I. D. Walker, "3d printing of concrete with a continuum robot hose using variable curvature kinematics," in *2022 International Conference on Robotics and Automation (ICRA)*. IEEE, 2022, pp. 3216–3222.

[29] M. Goharimanesh, A. Mehrkish, and F. Janabi-Sharifi, "A fuzzy reinforcement learning approach for continuum robot control," *Journal of Intelligent & Robotic Systems*, vol. 100, no. 3, pp. 809–826, 2020.

[30] P. Rao, Q. Peyron, and J. Burgner-Kahrs, "Shape representation and modeling of tendon-driven continuum robots using euler arc splines," *IEEE Robotics and Automation Letters*, vol. 7, no. 3, pp. 8114–8121, 2022.

[31] C. Yang, S. Geng, I. Walker, D. T. Branson, J. Liu, J. S. Dai, and R. Kang, "Geometric constraint-based modeling and analysis of a novel continuum robot with Shape Memory Alloy initiated variable stiffness," *Int. J. Rob. Res.*, 2020.

[32] B. Zhao, L. Zeng, Z. Wu, and K. Xu, "A continuum manipulator for continuously variable stiffness and its stiffness control formulation," *Mech. Mach. Theory*, vol. 149, 2020.

[33] Y. Wang, H. W. Yip, H. Zheng, H. Lin, R. H. Taylor, and K. W. S. Au, "Design and experimental validation of a miniaturized robotic tendon-driven articulated surgical drill for enhancing distal dexterity in minimally invasive spine fusion," *IEEE/ASME Transactions on Mechatronics*, vol. 26, pp. 1858–1866, 8 2021.

[34] S. H. Sadati, S. E. Naghibi, A. Shiva, B. Michael, L. Renson, M. Howard, C. D. Rucker, K. Althoefer, T. Nanayakkara, S. Zschaler *et al.*, "Tmtdyn: A matlab package for modeling and control of hybrid rigid–continuum robots based on discretized lumped systems and reduced-order models," *The International Journal of Robotics Research*, vol. 40, no. 1, pp. 296–347, 2021.

[35] B. Rong, X. Rui, L. Tao, and G. Wang, "Theoretical modeling and numerical solution methods for flexible multibody system dynamics," *Nonlinear Dynamics*, vol. 98, no. 2, pp. 1519–1553, 2019.

[36] A. Gao, J. Li, Y. Zhou, Z. Wang, and H. Liu, "Modeling and Task-Oriented Optimization of Contact-Aided Continuum Robots," *IEEE/ASME Trans. Mechatronics*, vol. 25, no. 3, pp. 1444–1455, 2020.

[37] G. Fang, C. D. Matte, R. B. Scharff, T. H. Kwok, and C. C. Wang, "Kinematics of Soft Robots by Geometric Computing," *IEEE Trans. Robot.*, vol. 36, no. 4, pp. 1272–1286, 2020.

Qingxiang Zhao received the B.Eng. degree and the M.S. degree in mechanical engineering from Sichuan University, Chengdu, China, in 2016 and 2019, respectively. In 2022, he obtained Ph.D. in mechanical engineering from the Hong Kong Polytechnic University. He is currently working as an Assistant Professor in Centre for Artificial Intelligence and Robotics (CAIR) Hong Kong Institute of Science & Innovation, Chinese Academy of Sciences. His research interests include soft robotics, industrial automation, and artificial intelligence.

Shuai Wang received the B.Eng. degree in mechatronics engineering from the Tianjin University of Science and Technology, Tianjin, China, in 2019, and the M.S. degree in mechanical engineering from The Hong Kong Polytechnic University, Hong Kong, China, in 2023. He is an Engineer with the Centre for Artificial Intelligence and Robotics (CAIR), Hong Kong Institute of Science and Innovation, Chinese Academy of Sciences, Hong Kong, China. His research interests include soft robotics, machine learning, robot trajectory planning and control.

Jian Hu received the B.Eng. degree in mechanical engineering from Tianjin University, Tianjin, China, M.S. degree in precision instrument and machinery from Beihang University, Beijing, China, and Ph.D degree in biomedical engineering from King's College London, London, UK, in 2013, 2016, and 2021, respectively. He is now an Assistant Professor with Institute of Automation, Chinese Academy of Sciences (CASIA), Beijing, China, and Centre for Artificial Intelligence and Robotics (CAIR), Hong Kong Institute of Science & Innovation, Chinese Academy of Sciences, Hong Kong, China. His research focuses on the development of medical robotic systems with advanced haptic perception.

Hongbin Liu is a Professor at Chinese Academy of Sciences, Institute of Automation (CASIA), Executive Director for the Centre of AI and Robotics (CAIR), Hong Kong Institute of Science & Innovation, Chinese Academy of Sciences. Dr Liu is also an adjunct Reader and director of the Haptic Mechatronics and Medical Robotics (HaMMeR) lab at the School of Biomedical Engineering and Imaging Sciences, King's College London (KCL), UK. Prof. Liu's group has been focusing on research and development of medical robotic systems with advanced haptic perception and interaction capabilities, to enable safer and more effective minimally invasive diagnosis and treatment for patients. Dr Liu's research has led to the clinical translation of a series of flexible robotic endoscopic systems for applications such as colonoscopy, bronchoscopy as well as vascular surgeries.

Henry K. Chu received the B.S. degree in mechanical engineering from the University of Waterloo, Waterloo, ON, Canada, and the M.S. and Ph.D. degrees in mechanical and industrial engineering from the University of Toronto, Toronto, ON, Canada. He was a Post-Doctoral Fellow with the University of Toronto and the City University of Hong Kong, Hong Kong. He is currently an Associate Professor with The Hong Kong Polytechnic University, Hong Kong. His research interests include robotic manipulation, vision-based control and automation, microsystem design, and tissue engineering.